




# Photonic response and temperature evolution of SiO<sub>2</sub>/TiO<sub>2</sub> multilayers

George Christidis<sup>1,\*</sup> , Olga B. Fabrichnaya<sup>2</sup>, Stefan M. Koepfli<sup>1</sup>, Erik Poloni<sup>3</sup>, Joel Winiger<sup>1</sup>, Yuriy M. Fedoryshyn<sup>1</sup>, Andrey V. Gusarov<sup>1</sup>, Mariia Ilatovskaia<sup>2</sup>, Ivan Saenko<sup>2</sup>, Galina Savinykh<sup>2</sup>, Valery Shklover<sup>1</sup>, and Juerg Leuthold<sup>1</sup>

<sup>1</sup>Institute of Electromagnetic Fields, ETH Zurich, Gloriastrasse 35, 8092 Zurich, Switzerland

<sup>2</sup>Institute of Material Sciences, Freiberg University of Mining and Technology, 09599 Freiberg, Germany

<sup>3</sup>Department of Materials, ETH Zurich, Complex Materials, 8093 Zurich, Switzerland

Received: 4 May 2021

Accepted: 23 September 2021

Published online:

7 October 2021

© The Author(s) 2021

## ABSTRACT

The microstructural and optical reflectivity response of photonic SiO<sub>2</sub>/TiO<sub>2</sub> nanomultilayers have been investigated as a function of temperature and up to the material system's melting point. The nanomultilayers exhibit high, broadband reflectivities up to 1350 °C with values that exceed 75% for a 1 μm broad wavelength range (600–1600 nm). The optimized nanometer sized, dielectric multilayers undergo phase transformations from anatase TiO<sub>2</sub> and amorphous SiO<sub>2</sub> to the thermodynamically stable phases, rutile and cristobalite, respectively, that alter their structural morphology from the initial multilayers to that of a scatterer. Nonetheless, they retain their photonic characteristics, when characterized on top of selected substrate foils. The thermal behavior of the nanometer sized multilayers has been investigated by differential thermal analysis (DTA) and compared to that of commercially available, mm-sized, annealed powders. The same melting reactions were observed, but the temperatures were lower for the nm-sized samples. The samples were characterized using X-ray powder diffraction before DTA and after annealing at temperatures of 1350 and 1700 °C. The microstructural evolution and phase compositions were investigated by scanning electron microscopy and energy-dispersive X-ray spectroscopy measurements. The limited mutual solubility of one material to another, in combination with the preservation of their optical reflectivity response even after annealing, makes them an interesting material system for high-temperature, photonic coatings, such as photovoltaics, aerospace re-entry and gas turbines, where ultra-high temperatures and intense thermal radiation are present.

Handling Editor: Christopher Blanford.

Address correspondence to E-mail: george.christidis@ief.ee.ethz.ch

## Introduction

High-temperature photonic materials are attracting more and more attention for applications where thermal stability and optical response as a function of temperature are critical parameters. Among these materials, silicon dioxide ( $\text{SiO}_2$ ) and titanium dioxide ( $\text{TiO}_2$ ) have been extensively studied in the visible (VIS) and near-infrared (NIR) parts of the electromagnetic spectrum, since they are widely used in medicine [1, 2], photovoltaics [3, 4], electronics [5, 6] and optics [7–10]. Both oxides display low or no optical losses, they have a high refractive index contrast ( $\Delta n \sim 1$ ) in the aforementioned electromagnetic spectra and they can be deposited into multilayer coatings using a variety of fabrication methods and techniques.

Both  $\text{SiO}_2$  and  $\text{TiO}_2$  have high melting points (1710 °C and 1843 °C, respectively [11]) and experiments with post-annealed powder mixtures of them have proved that the materials are immiscible in solid state and have limited mutual solubility in liquid state [12, 13]. As a result, they constitute an attractive material couple for high-temperature photonic applications [14], particularly in solar technology [15–17], and have been prepared using different fabrication conditions and methods [18, 19]. At elevated temperature conditions, thermal energy alters the microstructure of each material (phase, density, grain size, etc.), leading to structures different than originally designed.  $\text{SiO}_2$  films transform from amorphous or quartz (low temperature) to cristobalite ( $\sim 900$ – $1400$  °C) upon heating depending on the initial crystallinity of the film [20, 21], while in some cases the metastable tridymite is observed especially in the presence of impurities [22, 23]. Conversely,  $\text{TiO}_2$  thin films transform from amorphous to metastable anatase (300–400 °C) and then convert to thermodynamically stable rutile ( $\sim 800$  °C) [24, 25]. Recent work has shown that when heated up, a  $\text{SiO}_2/\text{TiO}_2$  multilayer exhibits a slightly different microstructure behavior compared to that of single  $\text{SiO}_2$  or  $\text{TiO}_2$  films. The presence of  $\text{SiO}_2$  increases the phase transition temperature threshold of  $\text{TiO}_2$  and consequently higher temperatures are required to get rutile [26].

In the case of  $\text{TiO}_2$ , the phase change does not only lead to improved crystallinity, but also to a refractive index increase from 2.1 (amorphous) up to 2.5–2.7

(rutile) [27, 28], while  $\text{SiO}_2$  retains values close to 1.45 for both amorphous and crystalline films [29, 30]. A refractive index increase also affects  $\Delta n$  and thus the photonic response of the whole multilayer stack. This has already been verified for  $\text{SiO}_2/\text{TiO}_2$  multilayers heated up to 500 °C [9]. Upon further heating, a partial melting of the materials and a liquid phase separation is observed. When the temperature reaches values beyond the system's eutectic point ( $L = \text{SiO}_2 + \text{TiO}_2$ ,  $\sim 1550$  °C), the liquid, which is in equilibrium with pure solid  $\text{TiO}_2$ , can further dissolve  $\text{TiO}_2$  starting from a concentration of 6.3 mol. % (eutectic composition) and further up to  $\text{SiO}_2$  rich liquid in monotectic reaction (26.5 mol. %). In the monotectic reaction point (1780 °C), two liquids with compositions of 26.5 and 86 mol. %  $\text{TiO}_2$  coexist in equilibrium with rutile (monotectic reaction) [11, 31]. At temperatures above the monotectic reaction, two liquids coexist in equilibrium until the critical temperature is reached. The samples, which were held in miscibility gap composition range, typically formed  $\text{SiO}_2$  or  $\text{TiO}_2$  drops inside the other material's bulk matrix [31, 32]. The microstructure of the final samples is determined by the cooling rate, viscosity, density and interdiffusion of coexisting liquid phases. This high-temperature structural evolution and immiscibility of the  $\text{SiO}_2/\text{TiO}_2$  system makes it an interesting candidate as a photonic additives in thermal protection systems (TPS) and for elevated temperature applications such as thermo-photovoltaics [33], gas turbines [34, 35] and aerospace [36, 37], where high-flux radiation needs to be back-reflected in order to improve a systems' stability and performance.

Especially in the case of aerospace TPS, reflective photonic additives are required to address the high, incoming thermal radiation flux [38, 39]. This thermal radiation is the result of the space vehicle's hypersonic velocity during atmospheric entry, which heats up and ionizes the atmosphere's particles, leading to the formation of a bow shock layer [40]. The ionized particles emit high-intensity radiation at distinct wavelengths, which spread over broad wavelength ranges [41]. It is expected that future exploratory missions to planets like Mars and Venus will experience even higher thermal radiation loads, resulting from the spacecraft's increased weight and entry velocity [42, 43], and thus enhancing the TPS with photonic inclusions is a possible solution [37].

Recent in and ex situ thermal stability and high-temperature evolution studies have focused only on the mechanical properties of hard multilayer coatings [44–46]. Furthermore, the experiments have been conducted up to temperatures much lower than the melting points of these investigated materials.

In this work, we investigate the high-temperature microstructure evolution and photonic behavior of nanomultilayer SiO<sub>2</sub>/TiO<sub>2</sub> samples up to 1710 °C. It is shown that they can increase the diffuse reflectivity of absorbing or reflective substrates (e.g., graphite, tungsten) to values exceeding 75% across an almost 1000-nm-wide wavelength range. Further, it is found that the samples display similar microstructure behavior (grain size evolution, phase change temperatures, etc.) as commercially available mm-sized SiO<sub>2</sub>/TiO<sub>2</sub> powders despite their reduced size features. The successive heating of the nanomultilayers at a temperature of 1350 °C leads to phase transformations, which alter the original microstructure, but not their high reflectivity performance. On the contrary, the reflectivity remains close to the one originally measured. The presented experimental analysis provides a first insight on how microstructural changes affect the nanomultilayers' photonic response and the potential of the SiO<sub>2</sub>/TiO<sub>2</sub> material system for high-temperature stable, photonic additives.

## Experimental section

In this section, the fabrication, preparation and characterization (microstructure and optical response) of the SiO<sub>2</sub>/TiO<sub>2</sub> nanomultilayers and of the reference mm-sized, sintered SiO<sub>2</sub>/TiO<sub>2</sub> powder samples are briefly presented.

### Design and fabrication of nanomultilayer and reference material

A SiO<sub>2</sub>/TiO<sub>2</sub> nanomultilayer coating has been designed and optimized by means of an evolution strategy (ES) algorithm. The coating consists of 18 layers with individual layer thicknesses between 60–480 nm for both TiO<sub>2</sub> and SiO<sub>2</sub>. It has been optimized to provide high and broadband reflectivity in the visible and part of the NIR electromagnetic spectrum (700–1600 nm) as described in [37]. The

exact design of the coating can be found in the supplement.

The SiO<sub>2</sub>/TiO<sub>2</sub> nanomultilayers have been fabricated by Schott AG (Yverdon-Les-Bains, Switzerland) using e-beam deposition. A sacrificial, thin Al<sub>2</sub>O<sub>3</sub> layer (~ 500 nm) is firstly deposited between the Si substrate and the multilayer coating; Then, the SiO<sub>2</sub> and TiO<sub>2</sub> layers are successively deposited with controllable thickness (accuracy 1–2%) at a temperature of 300 °C and a deposition pressure lower than 10<sup>-6</sup> mbar. The nanomultilayers are detached from the Si substrate by chemically etching the Al<sub>2</sub>O<sub>3</sub> layer inside phosphoric acid (H<sub>3</sub>PO<sub>4</sub>) heated at 140 °C for 5 h. Following that, the solution's pH is neutralized using NaHCO<sub>3</sub>, and then it is filtered to collect the SiO<sub>2</sub>/TiO<sub>2</sub> nanomultilayers. The amount of coating, collected from a single 4" Si wafer, equals to approximately 30–32 mg. The acquired nanomultilayers are in a platelet-form with sizes that vary in diameter between 200–300 μm. This is due to the fact that the nanomultilayers are brittle and break into smaller pieces after their removal from the Si substrate.

The reference, mm-sized samples have been prepared by sintering powders of TiO<sub>2</sub> and SiO<sub>2</sub> at 1400 °C for a total sintering time of ~ 100 h. The sample has been characterized after the sintering using XRD and SEM/EDX. More specifically, a commercially available SiO<sub>2</sub> powder (Alfa Aesar, Germany) 99.995% purity having quartz structure, and a TiO<sub>2</sub> powder from the same producer, purity 99.990% in rutile crystalline form, have been used to create the reference sample. Both powders have a 40 mesh particle size (~ 0.4 mm).

### Microstructural characterization of materials

The thickness, morphology and microstructure of the deposited SiO<sub>2</sub>/TiO<sub>2</sub> nanomultilayers have been characterized with a Hitachi SU8230 field-emission scanning electron microscope (SEM). For this, the samples have been mechanically cleaved. Energy-dispersive X-ray spectroscopy (EDX) measurements have been performed in order to verify the layers' elemental composition.

The phase composition and crystallinity of the nanomultilayers have been determined by an X'Pert<sup>3</sup> Powder (Panalytical). Typical 2θ measurement scans have been performed at angles 2θ = 15°–85°, where the diffraction peaks of TiO<sub>2</sub> (anatase, rutile) and SiO<sub>2</sub>

(quartz, cristobalite) are located according to the literature.

The high-temperature behavior of the nanomultilayer samples has been analyzed using differential thermal analysis (DTA). To investigate the phase transformations of the nanomultilayers, two different DTA devices have been used. For temperatures below 1650 °C, a TG–DTA SETSYS Evolution-1750 (SETARAM Instrumentation, France) with a Pt/PtRh 10% thermocouple has been used. The ceramic specimens have been placed in open Pt crucibles, heated up to 1650 °C and cooled in air atmosphere, using a heating and cooling rate of 10 and 30 °C·min<sup>-1</sup>, respectively. DTA measurements at higher temperatures, up to 1850 °C, have been performed in a TG–DTA SETSYS Evolution-2400 (SETARAM Instrumentation, France) using open W crucibles and employing a permanent inert gas flow (He).

Likewise, the microstructure of the mm-sized, reference samples has been examined using a LEO 1530 Gemini, Carl Zeiss (SEM) equipped with an EDX detector (Bruker AXS Mikroanalysis GmbH). Its X-ray powder diffraction (XRD) measurements were performed with a URD63 (Seifert–FPM, Freiberg, Germany) diffractometer using CuK<sub>α</sub> radiation. In this case, a Rietveld analysis has also been made using MAUD software [47]. The high-temperature behavior of the reference sample was investigated for the sample containing 50 mol.% SiO<sub>2</sub> and 50 mol.% TiO<sub>2</sub> under the same temperature and atmosphere conditions. The only difference is that the reference sample has been heated up to 1950 °C in the TG–DTA SETSYS Evolution-2400 system.

## Results and discussion

### XRD characterization of as-deposited nanomultilayers & sintered, reference samples

In this section, we discuss the morphology, phase composition of the as-deposited SiO<sub>2</sub>/TiO<sub>2</sub> nanomultilayers, after detaching from the substrate, Fig. 1, and compare them to commercially available, sintered, mm-sized SiO<sub>2</sub>/TiO<sub>2</sub> powder samples, Fig. 2.

The evaporated, nanomultilayer samples consist of SiO<sub>2</sub> layers that present amorphous phase, and metastable, polycrystalline anatase TiO<sub>2</sub> layers. The

phase composition of the materials is in good agreement with previously published work, since both TiO<sub>2</sub> and SiO<sub>2</sub> have been evaporated at slightly elevated substrate temperature (~ 300 °C) [20, 48]. This deposition temperature is well below the crystallization temperature threshold of rutile TiO<sub>2</sub> (700–800 °C) and quartz SiO<sub>2</sub> (~ 800 °C). Nevertheless, the intensity of the measured anatase phase differ significantly with respect to the bulk anatase. This can be attributed to the preferred orientation the multilayer displays. This phenomenon has already been reported in the literature [49, 50] and occurs when the crystallites of a sample align parallel to the surface of the measurement holder. The Si peak at  $2\theta = 28.5^\circ$  can be attributed to small Si chip fragments originating from the substrate during the detaching of the coating from the wafer (cleaving into smaller pieces). In the next step, the Si fragments, which originate from the cleaving of the Si substrate before inserting the sample into the H<sub>3</sub>PO<sub>4</sub>, are removed from the suspension using suction filtration. The cleaving of Si into smaller pieces is necessary to speed up the wet etch process. The fragments themselves do not contribute to the photonic performance of the sample, but could contaminate it.

Figure 2a, b shows the microstructure and XRD pattern of the reference SiO<sub>2</sub> and TiO<sub>2</sub> powder, sintered at 1400 °C, for comparison. It can be concluded based on EDX measurements that there is no mutual solubility between TiO<sub>2</sub> and SiO<sub>2</sub>, i.e., rutile TiO<sub>2</sub> does not dissolve any SiO<sub>2</sub> and vice versa. The sintered sample displays distinct SiO<sub>2</sub> and TiO<sub>2</sub> regions with maximum dimensions up to approximately 40 μm. The microstructure of the annealed sample is in accordance with previous work [31] and stems from the immiscibility of the two materials. The sintered SiO<sub>2</sub>/TiO<sub>2</sub> sample does not exhibit distinct structural morphology features and the materials are already in their high-temperature, stable phases. It should be noted that this annealed, heterogeneous sample has grains with relative interfaces much larger than the nanomultilayer samples presented in Fig. 1a. An EDX analysis reveals that the reference, annealed oxide powder samples form μm-sized grains, when heated at 1400 °C, which consist of SiO<sub>2</sub> (8 vol. % quartz and 56 vol. % cristobalite) and 36 vol. % TiO<sub>2</sub> rutile. The results for both nanomultilayers and reference sample are summarized in Table 1.



**Figure 1** **a** Cross section of SiO<sub>2</sub>/TiO<sub>2</sub> nanomultilayers, as-deposited on a Si substrate **b** XRD pattern of nanomultilayers after detaching from the substrate. The indexing of anatase TiO<sub>2</sub> peaks is shown.

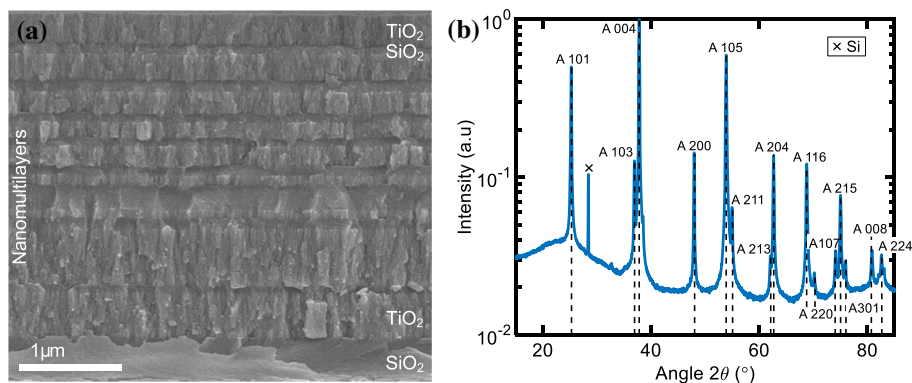


**Figure 2** Microstructure **a** and XRD pattern **b** of reference, oxide powder sample sintered at 1400 °C.

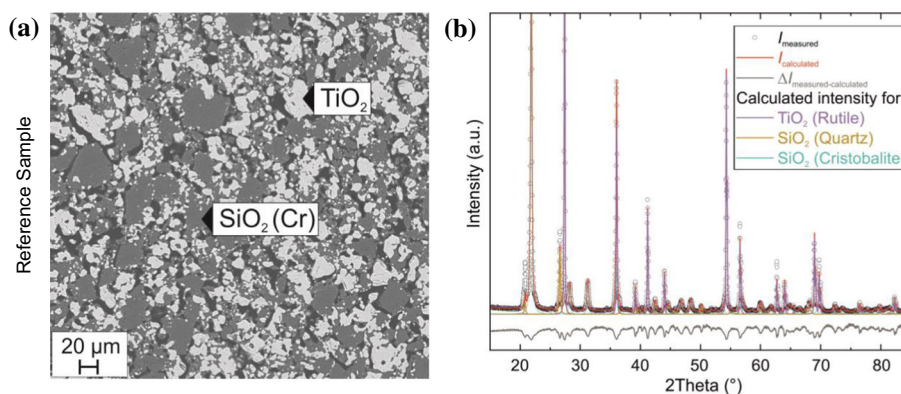


**Table 1** Weight ratio and vol. % of nanomultilayers and mm-sized, annealed powder sample

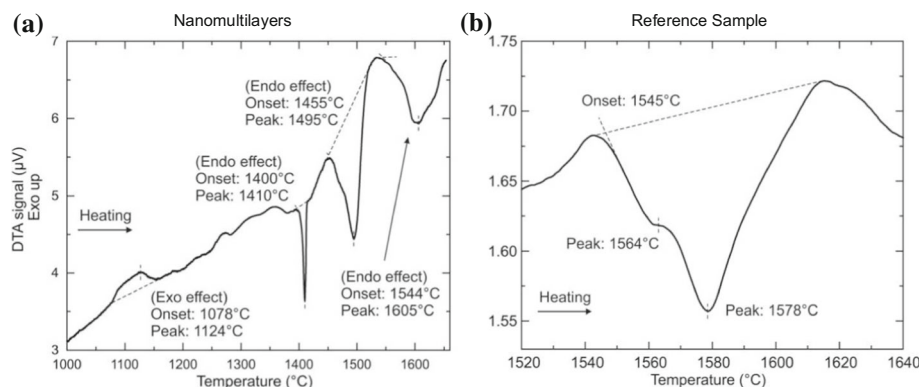
	SiO <sub>2</sub> layer – Weight ratio %	TiO <sub>2</sub> layer – Weight ratio %
Nanomultilayers	Si: 73.08 O: 26.92	Ti: 40.34 O: 55.64 Si: 4.02
Reference, sintered powders	SiO <sub>2</sub> – Vol. % Quartz: 8 Cristobalite: 56	TiO <sub>2</sub> – Vol. % Rutile: 36

### DTA and microstructure evolution as a function of temperature

A DTA for both samples has been performed in air atmosphere up to 1650 °C and in inert He atmosphere up to 1850 °C for the nanomultilayer sample and up to 1950 °C for the reference powder. For investigations up to 1650 °C, a Pt crucible in air atmosphere has been chosen. In order to investigate transformations above the melting point of Pt, tungsten crucibles have been used. Consequently, to avoid the oxidation of these W crucibles the experiments have been performed in inert gas atmosphere (He). The results of the DTA investigation for both sample in air are presented in Fig. 3a, b.

The DTA of the nanomultilayers, Fig. 3a, first reveals a wide exothermic effect in the temperature range between 1078 and 1150 °C, followed by an endothermic heat effect observed at a temperature of 1400 °C, a second larger endothermic effect at 1455 °C and a smaller third effect at 1544 °C. Conversely, the reference, sintered oxide sample only shows a broad, complex endothermic effect caused by at least two transformations. The temperature of the first onset was around 1545 °C, Fig. 3b. Using the phase diagram of the TiO<sub>2</sub>-SiO<sub>2</sub> system [31, 32], the first effect can be explained by the eutectic reaction (Liquid = SiO<sub>2</sub> + TiO<sub>2</sub>), followed by a continuous melting in two-phase field (Liquid + TiO<sub>2</sub>).

**Figure 3** Differential thermal analysis (DTA) curve of **a** nanomultilayer sample and of **b** reference, sintered sample heated up to 1650 °C.

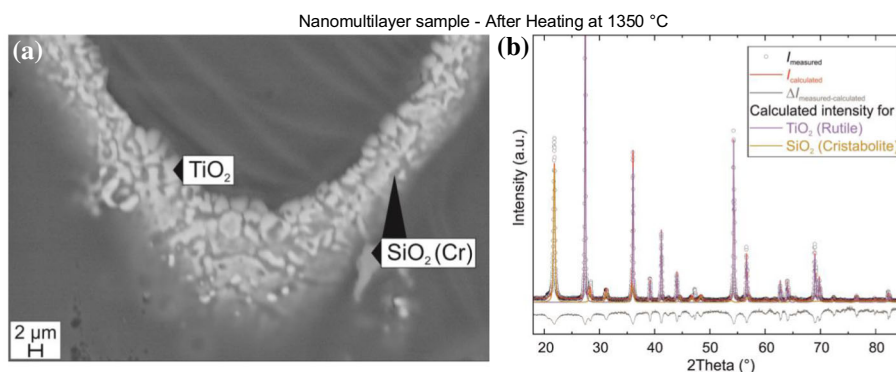


The exothermic effect of the nanomultilayers can be explained by the anatase to rutile transformation of  $\text{TiO}_2$  and the anticipated crystallization of amorphous  $\text{SiO}_2$  to quartz and cristobalite. In order to verify the origin of this exothermic effect the nanomultilayers are heat-treated at 1350 °C. The microstructure of scales obtained after heat treatment was investigated using SEM, Fig. 4a. The XRD pattern after heating is presented in Fig. 4b. The microstructure of the nanomultilayers shows that the nm layers have completely disappeared and  $\text{TiO}_2$  grains of approximately 2  $\mu\text{m}$  in size have formed inside a  $\text{SiO}_2$ -rich matrix. Additionally, separate  $\text{SiO}_2$  grains can be observed. The XRD pattern of the samples indicates the presence of rutile ( $\text{TiO}_2$ ) and cristobalite ( $\text{SiO}_2$ ), which are well fitted by Rietveld analysis. Additional diffraction peaks have been observed at  $2\theta = 28.5^\circ$  and  $2\theta = 48^\circ$ . These peaks have a higher intensity than the ones expected for cristobalite and do not correspond to the peak positions of  $\alpha$ -quartz ( $2\theta = 26.6^\circ$  and  $2\theta = 50^\circ$ ). Therefore, since no other elements except Ti, Si and O have been detected by EDX, these peaks can only be explained by the presence of metallic Si ( $2\theta = 28.1^\circ$  and  $2\theta = 47.4^\circ$ ). The presence of cristobalite indicates that

silicon dioxide melting did not occur, because after melting a  $\text{SiO}_2$ -rich, glassy-type amorphous phase would have formed. Glassy materials would appear as broad background peaks at low  $2\theta$  values in an XRD pattern. Hence, the exothermic effect is due to the phase transformation to the thermodynamically stable cristobalite ( $\text{SiO}_2$ ) and rutile ( $\text{TiO}_2$ ) phases. The temperature range in which these phase changes occurred is consistent with [26].

In the nanomultilayer sample one can further observe three endothermic peaks. The first and second heat effects are distinct and are observed at 1400 and 1455 °C, respectively, Fig. 3a. The third effect is less sharp and occurred at 1544 °C. We assume that the first endothermic peak (1400 °C) is due to the melting of Si. To confirm this assumption, the sample has been heat treated at 1420 °C and successively characterized by SEM and XRD. It is found that after the 1420 °C heat treatment, the XRD pattern is similar to the one obtained after the heat treatment at 1350 °C, presented in Fig. 4b, characterized by a higher intensity of peaks at  $2\theta = 28.5^\circ$  and  $2\theta = 48^\circ$ . It is possible that the Si distribution was not homogeneous in the sample and the portion heat treated at 1420 °C contained more Si. Hence, the Si chip traces,

**Figure 4 a** The microstructure of the multilayered sample after heat treatment at 1350 °C revealing  $\text{TiO}_2$  grains (white) in an  $\text{SiO}_2$  matrix (gray). The dark area, around the sample is resin. **b** XRD of the nanomultilayer sample after heat treatment at 1350 °C.



which had been initially detected by the XRD, have not oxidized during heating in DTA, even when heated at 1420 °C. However, after the heat treatment at 1650 °C Si does not remain in metallic state. It melts and becomes part of the SiO<sub>2</sub>/TiO<sub>2</sub> sample. Moreover, the microstructure of the nanomultilayers, heat-treated at 1420 °C, is similar to the one observed at 1350 °C, Fig. 4a. Consequently, the melting of Si has no effect on the nanomultilayer sample. The second heat effect at 1455 °C is related to the eutectic reaction Liquid = SiO<sub>2</sub> + TiO<sub>2</sub>. It should be noted that the onset temperature of this second effect is 90 °C lower in the nanomultilayer case than that of the reference, sintered sample, which has an onset of 1545 °C. This can be explained by the significantly smaller TiO<sub>2</sub> grains size in the multilayer sample compared to the sintered, reference powders. The third effect at 1544 °C in the multilayer sample can be explained by the continuous melting in two-phase Liquid + TiO<sub>2</sub>.

Figure 5a, b presents the DTA of the samples at a temperature of up to 1850 °C, under a He atmosphere. It shows a large endothermic effect at 1678 °C for the nanomultilayer and at 1706 °C for the sintered, reference sample.

The endothermic effects at 1678 °C (nanomultilayers) and 1706 °C (reference) can be explained by the liquid separation according to the monotectic reaction  $L_2 = L_1 + \text{TiO}_2$ . It should be noted that for both samples these heat effects have a quite complex structure and the difference in onset temperatures is less than 30 °C (~ 28 °C).

In order to better understand the thermal behavior of both samples, their microstructure after the heating in DTA has been investigated. Additionally, SEM images of both samples have been collected after heating up to the temperatures below or greater than

the onsets of heat effects observed in DTA, Fig. 6. More specifically, Fig. 6a presents the microstructure of the nanomultilayer sample after heating up to 1650 °C in DTA, while Fig. 6b shows the microstructure of the reference sample after heating in DTA under the same conditions. In both cases, TiO<sub>2</sub> grains inside a SiO<sub>2</sub>-rich matrix can be observed but with different sizes. In the nanomultilayers, the grains are substantially smaller (~ 2 μm) and homogeneously distributed in the SiO<sub>2</sub> matrix, Fig. 6a and inset, while in the reference sample the TiO<sub>2</sub> grains have sizes exceeding 10 μm, Fig. 6b. The much smaller grain sizes of the nanomultilayer sample can explain the difference in thermal behavior with the reference sample.

An SEM/EDX analysis of the samples' images after heating at 1650 °C, see Fig. 6a, shows that the white TiO<sub>2</sub> grains do not contain SiO<sub>2</sub> (~ 1 mol. %), while the dark SiO<sub>2</sub> areas contain TiO<sub>2</sub> corresponding to a eutectic composition (7 mol. % TiO<sub>2</sub>). This indicates that the TiO<sub>2</sub> grains, which were partially melted by the eutectic reaction  $\text{TiO}_2 + \text{SiO}_2 \rightarrow L_1$ , enriched the liquid with TiO<sub>2</sub>, while unmelted TiO<sub>2</sub> grains preserve their pure composition.

To understand the reason of the first effect observed during heating in DTA up to 1850 °C, the nanomultilayer sample was heated up to 1700 °C in DTA and held in that temperature for 600 s, Fig. 6c. A substantial change of microstructure can be observed. Large grains of TiO<sub>2</sub>, in the range approximately 20–70 μm, in a SiO<sub>2</sub>-rich matrix and small droplets of molten TiO<sub>2</sub> are present after this heat treatment. The grain size of TiO<sub>2</sub> is even higher than that of the reference sample heated up to 1650 °C, Fig. 6b. Upon further heating, the nanomultilayer sample exhibits a second heat effect at the same temperature as that of the reference sample (~ 1700

**Figure 5** **a** Differential thermal analysis (DTA) of nanomultilayers heated up to 1780 °C under a He atmosphere. **b** DTA curve of reference, sintered samples heated up to 1850 °C under the same conditions.

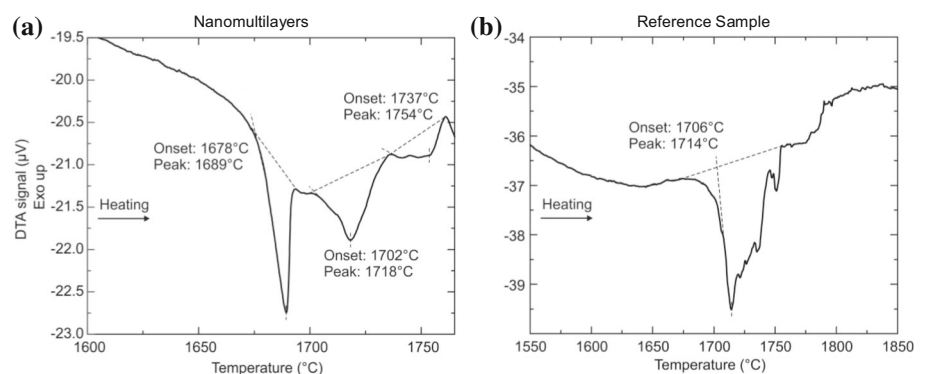
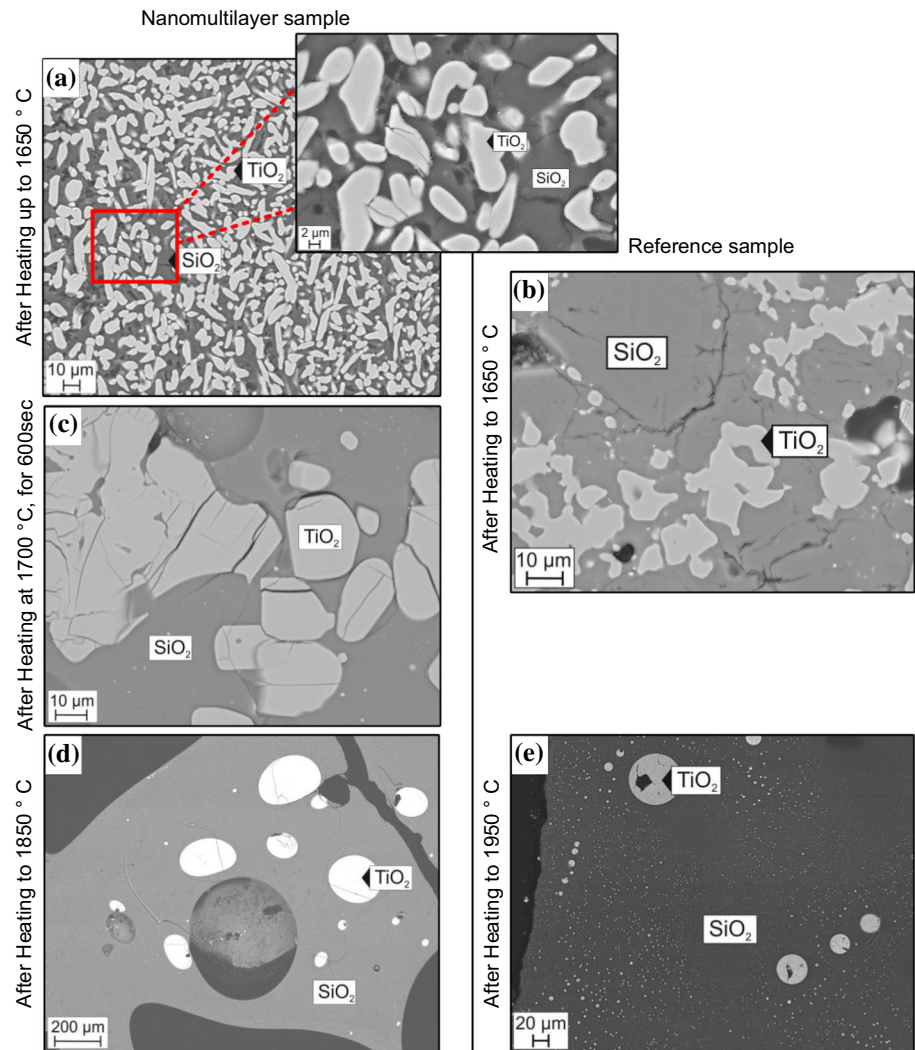


**Figure 6** **a** Microstructure of the nanomultilayer sample after heating up to 1650 °C in DTA and its inset. **b** Microstructure of reference, sintered sample heated up to 1650 °C **c** Nanomultilayers' microstructure after heat treatment at 1700 °C in DTA for 600 s. **d-e** Microstructure of the nanomultilayer sample after heating up to 1850 °C and of the reference sample after heating up to 1950 °C, respectively.



°C). This monotectic reaction first affects the small  $\text{TiO}_2$  grains, while at the same time unmelted  $\text{TiO}_2$  starts to form larger grains. Figure 6d shows that the monotectic reaction was completed upon heating the nanomultilayer sample up to 1850 °C. Microstructure characterization after heating up to 1850 °C for the nanomultilayers, Fig. 6d, and up to 1950 °C for the reference sample, Fig. 6e, indicates a similar microstructure that is typical of liquid separation for both samples. According to the SEM/EDX analysis a liquid separation occurred with the white drops of frozen  $\text{TiO}_2$ -rich liquid containing 10% mol.  $\text{SiO}_2$  and the dark  $\text{SiO}_2$ -rich liquid containing 16 mol. %  $\text{TiO}_2$ . It should be noted that the compositions of  $\text{TiO}_2$ -rich liquid and  $\text{SiO}_2$ -liquid were the same within uncertainty limits measured in the multilayer and in the reference sample.

### Optical response evolution of nanomultilayers as a function of temperature

In this section, we evaluate the photonic enhancement response of the  $\text{SiO}_2/\text{TiO}_2$  nanomultilayers as a function of temperature and microstructural change. Additional information about the sample's characteristics and optical microscopy images of them can be found in the supplement.

For the optical characterizations, the nanomultilayer flakes are mixed with ethanol and are being placed into cylindrical containers. The base of the container comprises a substrate (e.g., graphite, tungsten). After the ethanol has evaporated, the container is being removed. The sample ("cake") has a height of about ~ 2–2.2 mm and a radius of 6 mm. Then the "cake" is controllably brought to the bottom part of



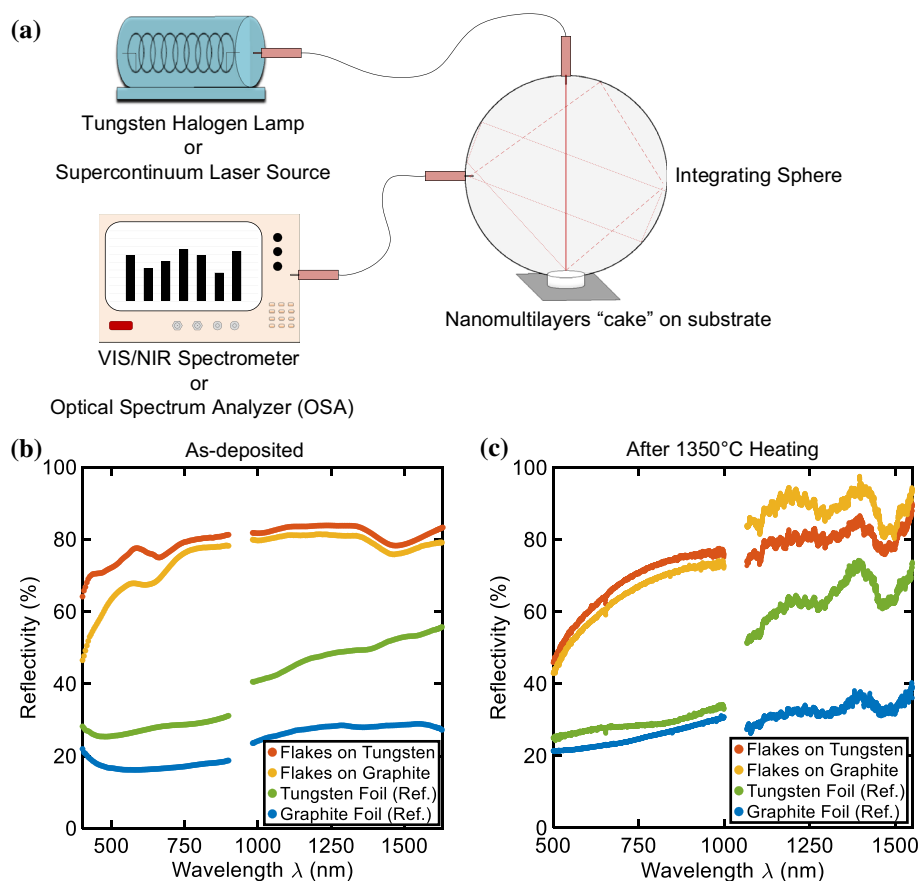
an integrating sphere (ISP-50-8-R – Ocean Insight), where its directional-hemispherical reflectivity is measured. More particularly, light generated from a tungsten-halogen lamp (HL-2000, Ocean Insight) or a supercontinuum laser source (SuperK Red, KOHERAS/NKT Photonics) is coupled to an optical fiber and illuminates the top of the sample. The scattered, reflected light is collected by a second optical fiber and is measured either at an optical spectrometer (Flame VIS–NIR Spectrometer, Ocean Insight / CCS200M, ThorLabs) or at an optical spectrum analyzer (OSA – Yokogawa AQ6370C). A diffuse reflectivity standard (WS1–PTFE, Ocean Insight) has been used as a reference in order to evaluate the directional-hemispherical reflectivity. A scheme of the used optical setup is shown in Fig. 7a. The photonic response of the powder is measured with different substrate bases having known optical properties. More specifically, we use tungsten, which is partially reflecting and absorbing and graphite, which is highly absorbing across the whole wavelength range of interest. Fig. 7b presents the as-deposited reflectivity of the nanomultilayers on top of

the two substrates, while Fig. 7c shows the reflectivity after heating up at 1350 °C. The pure substrate reflectivity is also provided as a reference.

The directional-hemispherical reflectivity of the nanomultilayer flakes and the substrate bases are plotted in Fig. 7b, c. Fig. 7(b) shows the photonic response at room temperature. It can be seen that the reflectivities of reference substrate, comprising a tungsten base or graphite base, increase from a value of ~ 26–56% (solid green line) and ~ 16–29% (solid blue line) to values close to 80%, when the flakes are added. The nanomultilayers exhibit a high reflectivity response in the range between 850 and ~ 1400 nm, which closely matches the window of interest for protection against thermal radiation during atmospheric re-entry (700–1600 nm). Their response does not display pronounced reflectivity dips (resonances), in the aforementioned range, and is relatively flat. The reflectivities of the materials measured at room temperature, see Fig. 7b, and the reflectivities of the materials after annealed at 1350 °C  $\text{SiO}_2/\text{TiO}_2$ , see Fig. 7c, show comparable values independent of the base substrate. The transformation of both  $\text{SiO}_2$

**Figure 7 a** Scheme of optical characterization setup utilizing an integrating sphere.

**b** Directional-hemispherical reflectivity measurements of the  $\text{SiO}_2/\text{TiO}_2$  nanomultilayers placed onto a tungsten base (red) and graphite base (orange) at room temperature and **c** after heating up to a temperature of 1350 °C as a function of wavelength. The reference reflectivities of the tungsten and graphene bases (without platelets) are shown by the solid green and blue lines.



and  $\text{TiO}_2$  into their thermodynamically stable phases at higher temperature leads to a material density change, which manifests as a change in the reflectivity response shown when going from Fig. 7b,c. Nevertheless, the overall performance of the samples does not dramatically change between the as-deposited and after heating up measurements. It should be noted that the characterization using an integrating sphere accounts for all different angles of incidence (directional–hemispherical reflectivity) and as such any reflectivity dips or peaks are smoothed. The similarity of the reflectivity curves for both temperatures and substrate types, in combination with the intrinsic, optical properties even with different substrate bases, demonstrates that reflectivity is mainly the result of the multilayer powder and not the substrate bases. Therefore, it can be concluded that the optical thickness of the measured “cakes” is in each case much greater than unity. The slight absolute difference between the two reflectivity curves (nanomultilayers on graphite and tungsten) may be attributed to some randomness in the surface morphologies of the “cakes”, measurement inaccuracies and variations in the positioning of the “cake” at the opening of the integrating sphere, supplement. These morphological variances are due to the fact that the nanomultilayers are originally in a fine powder form (as-deposited) and in a grainy powder form (after heating at 1350 °C). Consequently, they exhibit high electrostatic forces, are brittle and require the use of ethanol for handling (“cake” preparation and transfer from one substrate to another). As a result, even though the “cake” samples appear similar in shape, thickness and morphology, they are not identical to one another during consecutive measurements on different substrates and at different temperatures. Another important point is that the two samples, as-deposited and after heating at 1350 °C, have been measured in different characterization setups, using a variety of sources and detectors. To that extent, some experimental error is expected as for example with the tungsten foil reflectivity, which shows a “jump” around 1  $\mu\text{m}$  (green curve). Even though similar behavior has been observed in literature for tungsten [51, 52], in our case the change is more pronounced and it can be attributed to additional measuring error found in both as-deposited and heated sample. Additionally, there is a profound ripple effect present in the NIR part of the

spectrum of the heated at 1350 °C sample due to the supercontinuum laser source.

## Conclusions

The high-temperature characteristics of  $\text{SiO}_2/\text{TiO}_2$  nanomultilayers demonstrated that the materials are interesting as a photonic additives for next generation photonically enhanced TPS. In view of this application, the microstructural and photonic response evolution of  $\text{SiO}_2/\text{TiO}_2$  nanomultilayers, have been investigated as a function of heating temperature. It has been shown that a powder of  $\text{SiO}_2/\text{TiO}_2$  nanomultilayers has increased the diffuse reflectivity of the underlying substrate base to values exceeding 75% across the whole VIS and part of the NIR electromagnetic spectrum. This has been proven independent of the used substrate, i.e., the same photonic performance is observed for a highly absorbing (graphite) or a weak reflecting (tungsten) substrate base. The nanomultilayers retain their optical characteristics upon heating up to 1350 °C, despite the microstructure changes they undergo when heated. This microstructural evolution with temperature is barely dependent on their reduced grain size and exhibits lower phase transitions temperatures to that of the reference, sintered at 1400 °C commercially available mm-sized powder. This has been verified by DTA, SEM/EDX and XRD characterization. The  $\text{SiO}_2$  and  $\text{TiO}_2$  immiscibility to one another in solid state and liquid separation with limited mutual solubilities, in combination with their thermal, microstructural behavior, constitute a prospective material system for the large scale fabrication of photonic additives that can be prepared by a variety of methods and techniques in quantities and dimensions compatible with TPS technology. These  $\text{SiO}_2/\text{TiO}_2$  nanomultilayers are engineered to possess desired photonic responses in desired wavelength bands at both low and high temperatures, making them a better option compared to commercial powders.

## Acknowledgements

This work has been financially supported by the Swiss National Science Foundation (project 200021\_160184, “Design and manufacturing of

heterogeneous photonic composites for aerospace applications”). The authors would like to thank the Cleanroom Operations Team of the Binnig and Rohrer Nanotechnology Center (BRNC) for their help and support, Schott AG (Yverdon-Les-Bains) for the fabrication of the SiO<sub>2</sub>/TiO<sub>2</sub> nanomultilayers., Thomas Weber (Roentgen Platform of Department of Materials of ETZ Zurich) for his aid in the XRD characterization and Dr. Martin Kotyrba (Laboratory of Chemistry and Applied Biosciences, ETH Zurich) for his assistance and technical support in the heating of the samples.

## Funding

Open Access funding provided by ETH Zurich.

## Declarations

**Conflict of interest** All authors declare that they have no competing financial interests or personal relationships that could have appeared to influence the work reported in this paper.

**Supplementary Information:** The online version contains supplementary material available at <http://doi.org/10.1007/s10853-021-06557-y>.

**Open Access** This article is licensed under a Creative Commons Attribution 4.0 International License, which permits use, sharing, adaptation, distribution and reproduction in any medium or format, as long as you give appropriate credit to the original author(s) and the source, provide a link to the Creative Commons licence, and indicate if changes were made. The images or other third party material in this article are included in the article’s Creative Commons licence, unless indicated otherwise in a credit line to the material. If material is not included in the article’s Creative Commons licence and your intended use is not permitted by statutory regulation or exceeds the permitted use, you will need to obtain permission directly from the copyright holder. To view a copy of this licence, visit <http://creativecommons.org/licenses/by/4.0/>.

**Supplementary Information:** The online version contains supplementary material available at <http://doi.org/10.1007/s10853-021-06557-y>.

## References

- [1] Pimenta S, Cardoso S, Miranda A, De Beule P, Castanheira EMS, Minas G (2015) Design and fabrication of SiO<sub>2</sub>/TiO<sub>2</sub> and MgO/TiO<sub>2</sub> based high selective optical filters for diffuse reflectance and fluorescence signals extraction. *Biomed Opt Express* 6(8):3084–3098. <https://doi.org/10.1364/BOE.6.003084>
- [2] Belcarz A, Bienias J, Surowska B, Ginalska G (2010) Studies of bacterial adhesion on TiN, SiO<sub>2</sub>–TiO<sub>2</sub> and hydroxyapatite thin layers deposited on titanium and Ti6Al4V alloy for medical applications. *Thin Solid Films* 519(2):797–803. <https://doi.org/10.1016/j.tsf.2010.08.117>
- [3] Lien S-Y, Wu D-S, Yeh W-C, Liu J-C (2006) Tri-layer antireflection coatings (SiO<sub>2</sub>/SiO<sub>2</sub>–TiO<sub>2</sub>/TiO<sub>2</sub>) for silicon solar cells using a sol–gel technique. *Sol Energy Mater Sol Cells* 90(16):2710–2719. <https://doi.org/10.1016/j.solmat.2006.04.001>
- [4] O’Sullivan F, Celanovic I, Jovanovic N, Kassakian J, Akiyama S, Wada K (2005) Optical characteristics of one-dimensional Si/SiO<sub>2</sub> photonic crystals for thermophotovoltaic applications. *J Appl Phys* 97(3):033529. <https://doi.org/10.1063/1.1849437>
- [5] Radecka M, Zakrzewska K, Czernastek H, Stapiński T, Debrus S (1993) The influence of thermal annealing on the structural, electrical and optical properties of TiO<sub>2</sub>-x thin films. *Appl Surf Sci* 65:227–234. [https://doi.org/10.1016/0169-4332\(93\)90663-V](https://doi.org/10.1016/0169-4332(93)90663-V)
- [6] Tang Y, Ao D, Li W, Zu X, Li S, Fu YQ (2018) NH<sub>3</sub> sensing property and mechanisms of quartz surface acoustic wave sensors deposited with SiO<sub>2</sub>, TiO<sub>2</sub>, and SiO<sub>2</sub>-TiO<sub>2</sub> composite films. *Sens Actuators, B Chem* 254:1165–1173. <http://doi.org/10.1016/j.snb.2017.07.195>
- [7] Tohru H, Katsunori Y, Junji Y, Hiroshi K, Fumio K, Kenichi I (1994) Fabrication of a ZnSe-Based Vertical Fabry-Perot Cavity using SiO<sub>2</sub>/TiO<sub>2</sub> multilayer reflectors and resonant emission characteristics. *Jpn J Appl Phys* 33(7R):3960–3961. <https://doi.org/10.1143/JJAP.33.3960>
- [8] Jiang K, Zakutayev A, Stowers J, Anderson MD, Tate J, McIntyre DH, Johnson DC, Keszler DA (2009) Low-temperature, solution processing of TiO<sub>2</sub> thin films and fabrication of multilayer dielectric optical elements. *Solid State Sci* 11(9):1692–1699. <https://doi.org/10.1016/j.solidstatesciences.2009.05.026>
- [9] Jena S, Tokas RB, Thakur S (1832) Sahoo NK (2017) Influence of annealing on optical, microstructural and laser induced damage properties of TiO<sub>2</sub>/SiO<sub>2</sub> multilayer high reflection mirror. *AIP Conf Proc* 1:060005. <https://doi.org/10.1063/1.4980410>

- [10] Bellum J, Field E, Kletecka D, Long F (2014) Reactive ion-assisted deposition of e-beam evaporated titanium for high refractive index TiO<sub>2</sub> layers and laser damage resistant, broad bandwidth, high-reflection coatings. *Appl Opt* 53(4):A205–A211. <https://doi.org/10.1364/AO.53.00A205>
- [11] DeVries RC, Roy R, Osborn EF (1955) Phase Equilibria in the System CaO-TiO<sub>2</sub>-SiO<sub>2</sub>. *J Am Ceram Soc* 38(5):158–171. <https://doi.org/10.1111/j.1151-2916.1955.tb14922.x>
- [12] McTaggart DG, Andrews AI (1957) Immiscibility area in the system TiO<sub>2</sub>-ZrO<sub>2</sub>-SiO<sub>2</sub>. *J Am Ceram Soc* 40(5):167–170. <https://doi.org/10.1111/j.1151-2916.1957.tb12596.x>
- [13] DeVries RC, Roy R, Osborn EF (1954) The system TiO<sub>2</sub>-SiO<sub>2</sub>. *Trans Brit Ceram Soc* 53(9):525–540
- [14] Yepuri V, Dubey RS, Kumar B (2020) Rapid and economic fabrication approach of dielectric reflectors for energy harvesting applications. *Sci Rep* 10(1):15930. <https://doi.org/10.1038/s41598-020-73052-w>
- [15] Yepuri V, Dubey DRS, Kumar B (2020) Fabrication and characterization of spectrally selective glazing dielectric multilayer structures. *Nanosystems Physics Chemistry Mathematics*. 11:488–492. <https://doi.org/10.17586/2220-8054-2020-11-4-488-492>
- [16] Dubey RS, Ganesan V (2018) Visible and near-infrared wavelength-selective dielectric reflectors for light management applications. *Superlattices Microstruct* 122:228–234. <https://doi.org/10.1016/j.spmi.2018.08.005>
- [17] Kim J, Baek S, Park JY, Kim KH, Lee J-L (2021) Photonic multilayer structure induced high near-infrared (NIR) blockage as energy-saving window. *Small* 17(29):2100654. <https://doi.org/10.1002/sml.202100654>
- [18] Guo C, Kong M (2020) Fabrication of ultralow stress TiO<sub>2</sub>/SiO<sub>2</sub> optical coatings by plasma ion-assisted deposition. *Coatings* 10(8):720. <https://doi.org/10.3390/coatings10080720>
- [19] Todea M, Pop-Muresan M, Simon S, Eniu D (2018) Thermal stability of anatase phase nanostructured in long time matured sol-gel derived TiO<sub>2</sub>-SiO<sub>2</sub> composite. *Optoelectron Adv Mater-Rapid Commun* 12(5–6):342–346
- [20] Tokuda T (1957) Crystallization of quartz at high temperatures. *Bull Chem Soc Jpn* 30(7):692–693. <https://doi.org/10.1246/bcsj.30.692>
- [21] Wahl FM, Grim RE, Graf RB (1961) Phase transformations in silica as examined by continuous x-ray diffraction. *Am Miner* 46(1–2):196–208
- [22] Novakovic R, Radic SM, Ristic MM (1986) Kinetics and Mechanism of Quartz-Tridymite Transformation. *Inter-Ceram: International Ceramic Review*. 15:29–30
- [23] Swamy V, Saxena SK, Sundman B, Zhang J (1994) A thermodynamic assessment of silica phase diagram. *J. Geophys. Res: Solid Earth* 99(B6):11787–11794. <https://doi.org/10.1029/93jb02968>
- [24] Amor SB, Guedri L, Baud G, Jacquet M, Ghedira M (2003) Influence of the temperature on the properties of sputtered titanium oxide films. *Mater Chem Phys* 77(3):903–911. [https://doi.org/10.1016/S0254-0584\(02\)00189-X](https://doi.org/10.1016/S0254-0584(02)00189-X)
- [25] Nakaruk A, Ragazzon D, Sorrell CC (2010) Anatase–rutile transformation through high-temperature annealing of titania films produced by ultrasonic spray pyrolysis. *Thin Solid Films* 518(14):3735–3742. <https://doi.org/10.1016/j.tsf.2009.10.109>
- [26] Wang X, Wu G, Zhou B, Shen J (2013) Thermal annealing effect on optical properties of Binary TiO<sub>2</sub>-SiO<sub>2</sub> Sol-Gel coatings. *Materials* 6(1):76–84. <https://doi.org/10.3390/ma6010076>
- [27] Tanemura S, Miao L, Jin P, Kaneko K, Terai A, Nabatova-Gabain N (2003) Optical properties of polycrystalline and epitaxial anatase and rutile TiO<sub>2</sub> thin films by rf magnetron sputtering. *Appl Surf Sci* 212–213:654–660. [https://doi.org/10.1016/S0169-4332\(03\)00015-1](https://doi.org/10.1016/S0169-4332(03)00015-1)
- [28] Tanemura S, Miao L, Wunderlich W, Tanemura M, Mori Y, Toh S, Kaneko K (2005) Fabrication and characterization of anatase/rutile-TiO<sub>2</sub> thin films by magnetron sputtering: a review. *Sci Technol Adv Mater* 6(1):11–17. <https://doi.org/10.1016/j.stam.2004.06.002>
- [29] Magnozzi M, Terreni S, Anghinolfi L, Uttiya S, Carnasciali MM, Gemme G, Neri M, Principe M, Pinto I, Kuo LC, Chao S, Canepa M (2018) Optical properties of amorphous SiO<sub>2</sub>-TiO<sub>2</sub> multi-nanolayered coatings for 1064-nm mirror technology. *Opt Mater* 75:94–101. <https://doi.org/10.1016/j.optmat.2017.09.043>
- [30] Kischkat J, Peters S, Gruska B, Semtsiv M, Chashnikova M, Klinkmüller M, Fedosenko O, Machulik S, Aleksandrova A, Monastyrskiy G, Flores Y, Ted Masselink W (2012) Mid-infrared optical properties of thin films of aluminum oxide, titanium dioxide, silicon dioxide, aluminum nitride, and silicon nitride. *Appl Opt* 51(28):6789–6798. <https://doi.org/10.1364/AO.51.006789>
- [31] Kirillova SA, Almjashv VI, Gusarov VV (2011) Phase relationships in the SiO<sub>2</sub>-TiO<sub>2</sub> system. *Russ J Inorg Chem* 56(9):1464. <https://doi.org/10.1134/s0036023611090117>
- [32] DeCapitani C, Kirschen M (1998) A generalized multi-component excess function with application to immiscible liquids in the system CaO-SiO<sub>2</sub>-TiO<sub>2</sub>. *Geochim Cosmochim Acta* 62(23):3753–3763. [https://doi.org/10.1016/S0016-7037\(98\)00319-6](https://doi.org/10.1016/S0016-7037(98)00319-6)
- [33] Shklover V, Braginsky L, Witz G, Mishrikey M, Hafner C (2008) High-Temperature Photonic Structures. *Thermal Barrier Coatings, Infrared Sources and Other Applications*.



- Journal of Computational and Theoretical Nanoscience. 5 (5):862–893. <https://doi.org/10.1166/jctn.2008.2532>
- [34] Kelly MJ, Wolfe DE, Singh J, Eldridge J, Zhu D-M, Miller R (2006) Thermal barrier coatings design with increased reflectivity and lower thermal conductivity for high-temperature turbine applications. *Int J Appl Ceram Technol* 3(2):81–93. <https://doi.org/10.1111/j.1744-7402.2006.02073.x>
- [35] Gupta M, Curry N, Nylén P, Markocsan N, Vaßen R (2013) Design of next generation thermal barrier coatings — Experiments and modelling. *Surf Coat Technol* 220:20–26. <https://doi.org/10.1016/j.surfcoat.2012.09.015>
- [36] Komarevskiy N, Shklover V, Braginsky L, Hafner C, Lawson J (2012) Potential of glassy carbon and silicon carbide photonic structures as electromagnetic radiation shields for atmospheric re-entry. *Opt Express* 20(13):14189–14200. <https://doi.org/10.1364/OE.20.014189>
- [37] Christidis G, Koch U, Poloni E, Leo ED, Cheng B, Koepfli SM, Dorodnyy A, Bouville F, Fedoryshyn Y, Shklover V, Leuthold J (2020) Broadband, high-temperature stable reflector for aerospace thermal radiation protection. *ACS Appl Mater Interfaces* 12(8):9925–9934. <https://doi.org/10.1021/acsami.9b20753>
- [38] Milos FS, Chen YK, Squire TH, Brewer RA (1999) Analysis of Galileo probe heatshield ablation and temperature data. *J Spacecr Rocket* 36(3):298–306. <https://doi.org/10.2514/2.3465>
- [39] Winter M, Herdrich G (2008) Heat Shield Temperatures and Plasma Radiation Obtained from Spectroscopic Observation of the STARDUST Re-Entry in the Near-UV. Paper presented at the 46th AIAA Aerospace Sciences Meeting and Exhibit,
- [40] Howe JT (1985) Introductory aerothermodynamics of advanced space transportation systems. *J Spacecr Rocket* 22(1):19–26. <https://doi.org/10.2514/3.25705>
- [41] Grinstead J, Wilder M, Olejniczak J, Bogdanoff D, Allen G, Dang K, Forrest M (2008) Shock-Heated Air Radiation Measurements at Lunar Return Conditions. Paper presented at the 46th AIAA Aerospace Sciences Meeting and Exhibit,
- [42] Brandis A, Johnston C, Cruden B, Prabhu D, Bose D (2012) Validation of High Speed Earth Atmospheric Entry Radiative Heating from 9.5 to 15.5 km/s. Paper presented at the 43rd AIAA Thermophysics Conference,
- [43] Grinstead JH, Wright MJ, Bogdanoff DW, Allen GA (2009) Shock Radiation Measurements for Mars Aerocapture Radiative Heating Analysis. *J Thermophys Heat Transfer* 23(2):249–255. <https://doi.org/10.2514/1.37281>
- [44] Aschauer E, Sackl S, Schachinger T, Bolvardi H, Arndt M, Polcik P, Riedl H, Mayrhofer PH (2018) Atomic scale investigations of thermally treated nano-structured Ti-Al-N/Mo-Si-B multilayers. *Surf Coat Technol* 349:480–487. <https://doi.org/10.1016/j.surfcoat.2018.06.026>
- [45] Riedl H, Aschauer E, Koller CM, Polcik P, Arndt M, Mayrhofer PH (2017) Ti-Al-N/Mo-Si-B multilayers: an architectural arrangement for high temperature oxidation resistant hard coatings. *Surf Coat Technol* 328:80–88. <https://doi.org/10.1016/j.surfcoat.2017.08.032>
- [46] Raab R, Koller CM, Koložvári S, Ramm J, Mayrhofer PH (2018) Thermal stability of arc evaporated Al-Cr-O and Al-Cr-O/Al-Cr-N multilayer coatings. *Surf Coat Technol* 352:213–221. <https://doi.org/10.1016/j.surfcoat.2018.08.002>
- [47] Lutterotti L, Matthies S, Wenk H MAUD (Material Analysis Using Diffraction): a user friendly Java program for Rietveld Texture Analysis and more. In: *Proceeding of the Twelfth International Conference on Textures of Materials (ICO-TOM-12)*, 1999. 1599
- [48] Hasan MM, Haseeb ASMA, Saidur R, Masjuki HH, Hamdi M (2010) Influence of substrate and annealing temperatures on optical properties of RF-sputtered TiO<sub>2</sub> thin films. *Opt Mater* 32(6):690–695. <https://doi.org/10.1016/j.optmat.2009.07.011>
- [49] Holder CF, Schaak RE (2019) Tutorial on powder X-ray diffraction for characterizing nanoscale materials. *ACS Nano* 13(7):7359–7365. <https://doi.org/10.1021/acsnano.9b05157>
- [50] Pecharsky VK, Zavalij PY (2009) *Fundamentals of Powder Diffraction and Structural Characterization of Materials*. 2nd edn. Springer, Boston, MA. <https://doi.org/10.1007/978-0-387-09579-0>
- [51] Minissale M, Pardanaud C, Bisson R, Gallais L (2017) The temperature dependence of optical properties of tungsten in the visible and near-infrared domains: an experimental and theoretical study. *Journal of Physics D: Applied Physics* 50(45):455601. <https://doi.org/10.1088/1361-6463/aa81f3>
- [52] Walsh TA, Bur JA, Kim Y-S, Lu T-M, Lin S-Y (2009) High-temperature metal coating for modification of photonic band edge position. *J Opt Soc Am B*. 26(7):1450–1455. <https://doi.org/10.1364/JOSAB.26.001450>

**Publisher's Note** Springer Nature remains neutral with regard to jurisdictional claims in published maps and institutional affiliations.